# The Delicate Balance of Phase Speciation in Bimetallic Nickel Cobalt Nanoparticles

Alberto Palazzolo, Cyprien Poucin, Alexy Freitas, Anthony Ropp, Corinne Bouillet, Ovidiu Ersen, Sophie Carenco

# The Delicate Balance of Phase Speciation in Bimetallic Nickel Cobalt Nanoparticles

*Alberto Palazzolo,[1] Cyprien Poucin,[1] Alexy P. Freitas,[1] Anthony Ropp,[1] Corinne Bouillet,[2] Ovidiu Ersen,[2] Sophie Carenco,[1,*]*

[1] Sorbonne Université, CNRS, Collège de France, Laboratoire de Chimie de la Matière Condensée de Paris, 4 place Jussieu, 75005 Paris, France

[2] Institut de Physique et Chimie des Matériaux de Strasbourg (IPCMS), UMR 7504 CNRS−Université de Strasbourg, 23 rue du Loess, BP 43, Strasbourg Cedex 2, France

E-mail: sophie.carenco@sorbonne-universite.fr

**Abstract:** Bimetallic nickel-cobalt nanoparticles are highly sought for their potential as catalytic and magnetic nanoparticles. These are typically prepared in organic solvents in the presence of strong stabilizing ligands such as tri-*n*-octylphosphine (TOP). Due to the variety of cobalt crystallographic phases and to the strong interaction of the ligands with the metallic surfaces, forming *fcc* nanoparticles rather than phase mixture is a challenging endeavor. Here, using a two-step synthesis strategy that aims at a core-shell nickel-cobalt morphology, we demonstrated that many parameters have to be adjusted: concentration of the metal precursors, stoichiometry of TOP, and heating program from room temperature to 180 °C. We found optimized conditions to form size-controlled *fcc* NiCo nanoparticles from preformed Ni nanoparticles, and the phase attribution was confirmed with a combination of X-Ray diffraction on powder and X-Ray absorption spectroscopy at Co K edge. We then investigated the early stages of Co nucleation on the nickel using a lower stoichiometry of Co, down to 0.05 equiv. *vs.* Ni. Using X-ray photoelectron spectroscopy and scanning transmission electron microscopy coupled to energy-dispersive X-Ray spectroscopy and electron energy loss spectroscopy, we showed that cobalt reacts first on the nickel nanoparticles but easily forms cobalt-rich larger aggregates in the further steps of the reaction.

**Keywords:** bimetallic nanoparticles, colloidal synthesis, phase control, cobalt, nickel.

## 1. Introduction

The combination of two metals in a single nano-object is as interesting as challenging. Indeed, bimetallic nanoparticles have been widely studied during recent years because of the multiple possibilities which can rise from the interaction between the two components.[1] Alongside, in the fields of energy harvesting and catalysis, it is of paramount importance to shift from noble metals to first-row transition metals such as Ni, Cu, Co and Fe because of their lower cost and higher availability.[2] In this context, bimetallic nickel cobalt nanoparticles (NiCo NPs) have attracted the attention of the community thanks to the synergic catalytic activity of the combined metals. For example, NiCo NPs were used for the dry reforming of $CO_2$,[3–5] for hydrogen production,[6] for the depolymerization of lignin,[7] for hydrogen production,[8] and recently as catalysts for hydrosilylation.[9] Interestingly, the ratio of nickel to cobalt greatly affects the catalytic activity and the deactivation rate of the nanoparticles during a dry reforming of methane reaction.[10] Core-shell NiCo NPs were prepared by depositing cobalt on preformed nickel nanoparticles, and they were tested for the hydrogenation of carbon dioxide into carbon monoxide, methanol and formaldehyde, showing an interesting selectivity for oxygenated products.[11] Such selectivity could not be reached with pure Co or pure Ni nanoparticles. NiCo NPs modified with $PPh_3$ or P*n*$Bu_3$ ligands were also active for benzaldehyde reduction by silanes at room temperature.[9]

Despite the huge interest of NiCo NPs, synthesis of well-defined objects in composition, size and crystallinity is still a challenge. In particular, it is expected that core-shell nanoparticles will exhibit properties that differs from the alloyed ones, especially as several crystalline phase may coexist. While there are many reports of supported NiCo NPs,[5,12–15] synthetic path in one pot using colloidal routes seems more difficult to design. These can take advantage of the different reduction potential of Ni and Co,[16–24] of electroless deposition,[25] or of laser ablation[26] although they may end up being fairly aggregated[27] or poorly crystallized,[19]

or too crystallized to be attributed to nano-domains.[28] Few reports mention the possibility to form composition-controlled NiCo NPs.[29–31] Amongst them, the study by van Schooneveld et al. interestingly proposed a synthetic route in one pot, using a Ni(II) precursor and a Co(0) precursor with ratio that were systematically varied. This provided them with alloy of tunable composition, provided that acetone was used to dissolve the cobalt precursor, thus undergoing an intermediate acetonation reaction. Surprisingly, Co-rich reaction mixture led to even more Co-rich nanoparticles while Co-poor ones led to even more Co-poor nanoparticles.[29] In contrast with this study, Marusak et al. used Ni(II) and Co(II) precursors in three molar ratio (1.14, 2.28, 3.42) and they found that, under these conditions, Co was less efficiently introduced in the nanoparticles than Ni.[30] This generally raises the question of reaction yield vs. each metal and depending on the precursors and operating conditions.

Phase speciation was studied in few studies, keeping in mind that fcc Ni, Co and NiCo have close lattice parameters and are practically very hard to distinguish as soon as the crystallites are nano-sized. From a polyol route at 170 °C, both pure *hcp* and mixed *hcp+fcc* nano-crystalline phase were obtained for NiCo powders with various morphologies.[18] *fcc* NiCo NPs were obtained at 280 °C for Co/Ni ratio of 0.3 to 0.8, while *hcp* Ni or $\varepsilon$ Co were obtained with other ratio.[29] The phase affects the nature of the exposed facets, affecting the catalytic performances, as well as the electronic properties of the solid, as was demonstrated for the magnetic properties of Co, for instance.[32] As such, it is quite interesting to describe and control the phase in bimetallic nanoparticles as well.

In order to clarify the phase speciation in NiCo NPs and provide an alternative route to composition-controlled and size-controlled nanoparticles, we investigated the possibility to obtain them from preformed *fcc* Ni NPs prepared through a robust colloidal reaction.[33,34] We selected $Co_2(CO)_8$ as a cobalt source, at the suitable formal oxidation state (0) for avoiding redox reaction at the Ni surface and we investigated several Co/Ni ratio, from 1.0 to 0.05. We

investigated a range of operating conditions, varying the dilution, the stoichiometry of the main surface ligand (tri-*n*-octylphosphine) and the heating program, to finally obtain phase-pure *fcc* NPs. Lastly, we lowered the stoichiometry of the cobalt precursor to get an insight of the first stage of cobalt deposition on the Ni NPs surface. We then discuss the role of each parameter for the production of phase-pure and composition-controlled NPs, while delineating the limits of the proposed synthetic approach. Overall, the present work contributes to the topic of preparing phase-controlled *fcc* NiCo bimetallic nanoparticles while unveiling the challenge of suppressing the formation of the *hcp* phase in a robust manner.

## 2. Results

### 2.1 Sensitivity of the synthesis to process parameters

The starting point of this study is the protocol reported in a previous study.[11] Briefly, nickel nanoparticles (Ni NPs) are formed in a first step from dry nickel(II) acetylacetonate (acac) in the presence of 3 equiv. of tri-*n*-octylphosphine (TOP) and 12 equiv. of oleylamine (OAm), which acts both as solvent and reducing agent, at 220 °C for 2 h. In a second step, and without further treatment, the cobalt(0) precursor, $Co_2(CO)_8$ (one equiv. of Co *vs.* Ni), was added at room temperature and the mixture was heated up again. A first temperature step of 120 °C was kept for 20 min, to efficiently solubilize the cobalt precursor. As expected, we observed bubbling in the solution, due to the release of some CO molecules. Then the temperature was increased to 180 °C and kept for 1 h. Small nanoparticles of 12 nm diameter (Figure 1B) were obtained.

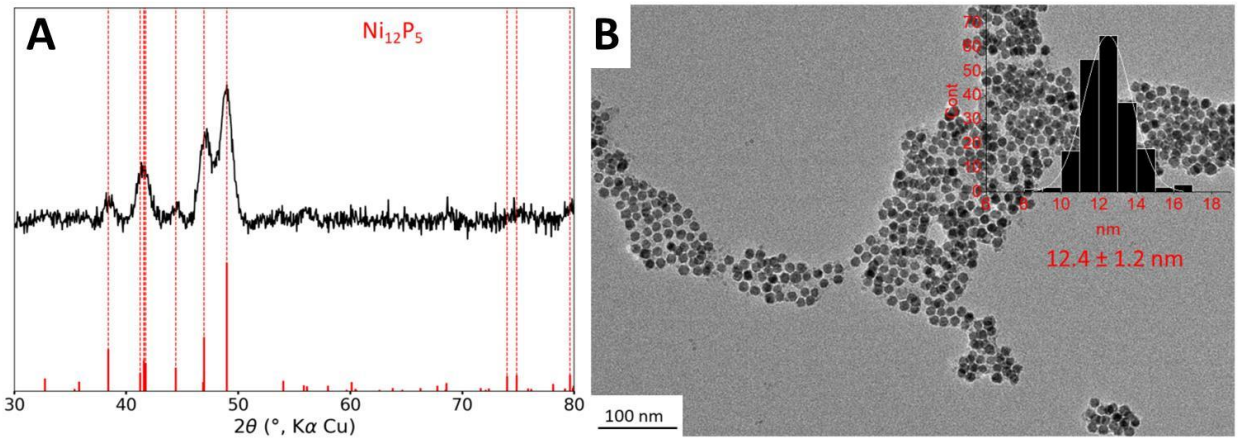


**Figure 1** (A) XRD pattern of the nanoparticles powder, the reference phase in red corresponds to $Ni_{12}P_5$ (PDF 03-065-4018, dotted lines are a guide to the eye). (B) TEM of the nanoparticles and size distribution in the inset.

Powder X-ray diffraction (XRD) was performed on the powder (Figure 1A). Broad peaks were detected corresponding to an average crystallite size of 10 nm according to the Scherrer relation. Interestingly, no cubic metallic phase was observed. Rather, the observed phase was isostructural to $Ni_{12}P_5$, which indicated that the nanoparticles were more phosphidized than anticipated. In fact, in the study published in 2015,[11] the STEM-EDS mapping of the

nanoparticles highlighted the presence of a cobalt-rich shell around a nickel-rich core, but the P K-edge mapping was not inconsistent with phosphorus inside the nanoparticle core. The presence of some phosphorus in the nanoparticle core, as phosphide species, can be explained due to the partial decomposition of the phosphine during the first step of the reaction (the synthesis of the nickel nanoparticles), as showed in a study published in 2017.[35] HRTEM did confirm the presence of nanoparticles with a crystalline core although the observations did not allow excluding the presence of an amorphous shell (Figure S3). This shell is not even in thickness and displays a non-regular TEM contrast: it could be made of cobalt/nickel (possibly oxidized due to air exposure) and/or carbon from the ligands.

Nanoparticles were smaller than these obtained in ref [11] (26 nm diameter in average). In order to confirm that this was not due to degradation of the particles after the addition of cobalt, the nanoparticles were isolated and analyzed after the first reaction step, that is, before cobalt was added. This step resulted in nanoparticles with a fairly sharp size distribution and an average diameter of 9 nm (Figure S2A), consistent with the size range expected in more diluted conditions reported in an earlier work.[33] We attribute this difference to the use of a different heating mantle and temperature controller setup, as well as a different TOP source, highlighting the well-known influence of process parameters on the outcome of the synthesis. Moreover, the nickel phosphidized phase could already be observed at this step by XRD (Figure S2B). In more diluted conditions reported in an earlier work, the nanoparticles were mostly amorphous.[33] This indicates that concentrated conditions are prone to favor the interaction of the phosphine with the nickel surface, and more phosphidation of the nanoparticles, in agreement with the interpretation proposed in the litterature.[36]

Besides, the presence of cobalt in the nanoparticles after the second step was confirmed by ensemble analysis: EDS performed at large scale on a SEM provided an average Co/Ni ratio of 0.5. X-Ray fluorescence spectroscopy on a pellet of the power confirmed the

Co/Ni ratio of 0.6. EDS performed at the scale of a single nanoparticle using a STEM instrument provided an average Co/Ni ratio of 0.6 (average on 6 locations), confirming the presence of cobalt in each nanoparticle. It appears that about 0.4 equiv. of cobalt did not enter or cover the nanoparticles. Rather, it was eliminated by the washing steps. In the previous study on larger nanoparticles, Co/Ni ratio of 1.0 was obtained, which will be discussed later.

The detection of phosphorus is trickier, because it is present in the remaining ligands in amounts that depend on the washing, and also because of the lower atomic number of this element. SEM-EDS provided a P/Ni ratio of 0.8 and STEM-EDS of 1.0. The difference likely comes from the amount of organics observed in each technique: at low magnification by SEM, an average of the powder is obtained, while STEM is performed on regions of the grids were the nanoparticles are best dispersed, which typically is promoted by a local excess of ligands.

Altogether, the nanoparticles produced here were composed of a nickel-rich phosphide core, likely surrounded by a cobalt-rich shell of poor crystallinity, not detected by XRD. The nanoparticles diameter was smaller than in the previous study, due to the first step of the formation of the nickel nanoparticles. The presence of a phosphorus-rich core was expected. A phosphide phase was detected, which was not expected but is still consistent with previous observations by STEM-EDS. This could be tamed by increasing the OAm/TOP ratio, based on previous works on nickel phosphides.[36] The cobalt incorporation at the second step was less efficient than expected, with final Co/Ni ratio lower than the expected value of 1.0, which suggested that some of the cobalt stayed trapped as a molecular species stabilized by TOP in solution.[37] This could be tamed by lowering the TOP stoichiometry, but also by favoring a better nucleation of cobalt as nanoparticle through a gentler heating ramp.

These unexpected results and the seemingly high sensitivity to the operating conditions let us to re-examine in detail the phase speciation in nickel-cobalt nanoparticles prepared by this

two-step route. Therefore, we decided to deeper investigate the influence of the synthesis parameters on the phase speciation, with the target of forming *fcc* NiCo nanoparticles, which is the expected phase at the reaction temperature.[38] We worked on the four actionable parameters mentioned above: (i) the dilution, (ii) the temperature ramp, (iii) the stoichiometry of the phosphine, (iv) the stoichiometry of cobalt.

### 2.2 Influence of dilution

Firstly, in order to hinder the formation of the phosphide phase, we used more diluted conditions. Increasing the amount of oleylamine to 22 equiv. led to the formation of nanoparticles with an average diameter of 12 nm, similar to these obtained above (Figure 2B). STEM-EDS mapping confirmed that each nanoparticle contained nickel and cobalt (Figure S4).

The absence of the crystalline phosphidized phase was confirmed by XRD, as observed on Figure 2A. However, we were puzzled to observe that, upon repetition, XRD measurements were not reproducible leading always to a metallic cubic phase and sometimes to an additional hexagonal phase (Figure 2A). For the cubic phase, the measured lattice parameter of $a$ = 3.526 Å can correspond to either *fcc* Ni ($a$ = 3.524 Å, JCPDS file 00-004-0850) or *fcc* NiCo alloy ($a$ = 3.534, JCPDS file 04-004-8490). For this reason and in the sake of clarity, all the following XRD patterns are displayed with the *fcc* Ni phase as the reference one. According to the Scherrer formula, the average crystallite size is 8 nm. The second set of broader diffraction peaks is attributable to an *hcp* cobalt phase (JCPDS file 04-001-3273) and it corresponds to an average crystallite size of 6 nm.

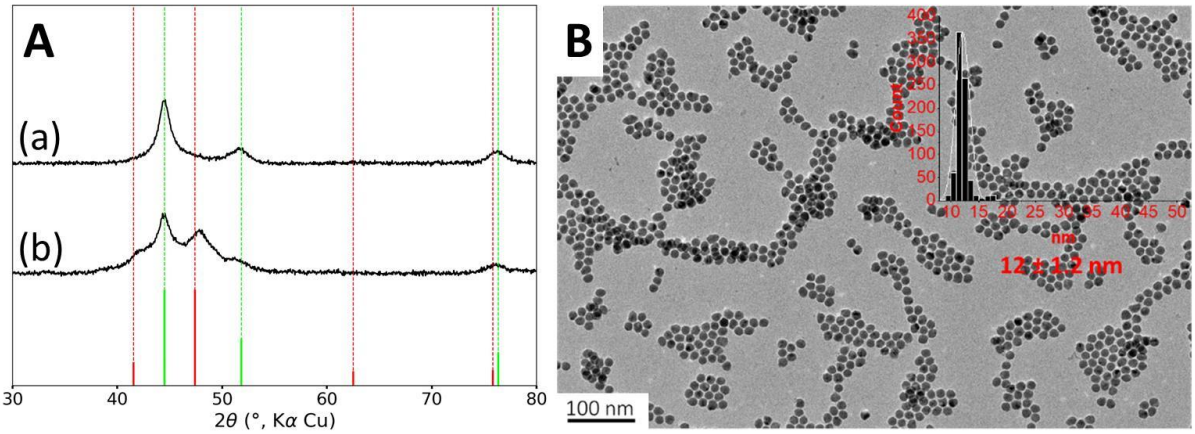


**Figure 2** (A) XRD pattern of two samples (a, b) prepared in diluted conditions, the reference phase in green corresponds to *fcc* Ni (JCPDS file 00-004-0850) and the reference phase in red corresponds to *hcp* cobalt (JCPDS file 04-001-3273). (B) Representative TEM of the nanoparticles and size distribution in the inset.

XRD sensitivity is limited when the crystallites are small and when the peaks partially overlap, which is the case here. The cubic pattern showed on Figure 2A-(a) may hide some lower amount of *hcp* phase. Deconvolution of the pattern did not allow detecting such *hcp* phase (Figure S15).

In order to confirm this, we used X-ray absorption spectroscopy (XAS), which probes the whole volume of the nanoparticle and is also sensitive to the local order. We recorded spectra in transmission mode at both Ni K-edge and Co K-edge for these *fcc* NiCo NPs and compared them with references compounds of metals and oxides. The X-ray absorption near edge structure (XANES) is presented on Figure 3A and Figure 3B for Ni and Co K-edges, respectively (the whole XAS is showed on Figure S8). We found that the edges of both Ni and Co were close to the metal reference edges indicating that most of their atoms were in a metallic environment and at an oxidation degree of 0. Regarding Ni K-edge (Figure 3A), the spectrum of the *fcc* NiCo NPs was much more similar to the spectrum of metallic Ni than to the spectrum of NiO. First, the edge position was measured at 8331 eV for the sample, when it was at 8332 eV for metallic Ni and 8343 eV for NiO, confirming the metallic character of the Ni atoms. Second, we noticed on Figure 3A that the oscillations in the extended X-Ray

absorption fine structure (EXAFS) region rapidly dampened after the white line. Still, their position matched with these of reference foil of metallic Ni but not with these of the NiO reference. In particular, there are (i) a local maximum at 8381 eV for both the sample and the metal Ni spectra, absent for the NiO spectrum and (ii) a lower absorption between 8394 and 8404 eV for both the sample and the metal Ni spectra, when the NiO spectrum presented a maximum at these energies. EXAFS at Co K-edge is presented on Figure 3C and D. It should be noted that the EXAFS spectra of bulk hexagonal and cubic Co are very similar.[39] Significant differences on the EXAFS spectra appear at $k > 13.5$ Å$^{-1}$, a value that cannot be exploited here because of the presence of nickel: Ni K-edge rises at *ca.* 8300 eV, which corresponds to $k = 12.5$ Å$^{-1}$ for cobalt. Here, we were able to collect data up to 10.5 Å$^{-1}$. At smaller *k*-values, two features can be used to discriminate between *hcp* or *fcc* phases, as shown Figure 3C on bulk references.[39] First, at *ca.* 6 Å$^{-1}$, a shoulder is expected for the *hcp* phase while the *fcc* phase presents a peak. Second, between 7.5 and 7.8 Å$^{-1}$ the observed decrease is twice more pronounced for the *fcc* phase (*ca.* 25% of the height of the peak at 8.1 Å$^{-1}$) than for the *hcp* phase (*ca.* 10% of the height of the peak at 8.1 Å$^{-1}$). The EXAFS spectrum of the NiCo NPs on Figure 3D (in black) was compared with these of a NiCo NPs powder (in violet) displaying both *fcc* and *hcp* phase by XRD. It presents a peak at 6 Å$^{-1}$ (rather than a shoulder), a strong decrease between 7.5 and 7.8 Å$^{-1}$ (ca. 30% of the height of the peak at 8 Å$^{-1}$). On the opposite, mixed phase compound has a shoulder at 6 Å$^{-1}$ and a small decrease between 7.5 and 7.8 Å$^{-1}$. Based on the interpretation extracted from the reference compounds of *fcc* Co and *hcp* Co, experimental observation of the two NiCo powders strengthens the trend observed by XRD, namely, the absence of the *hcp* phase in the black spectrum.

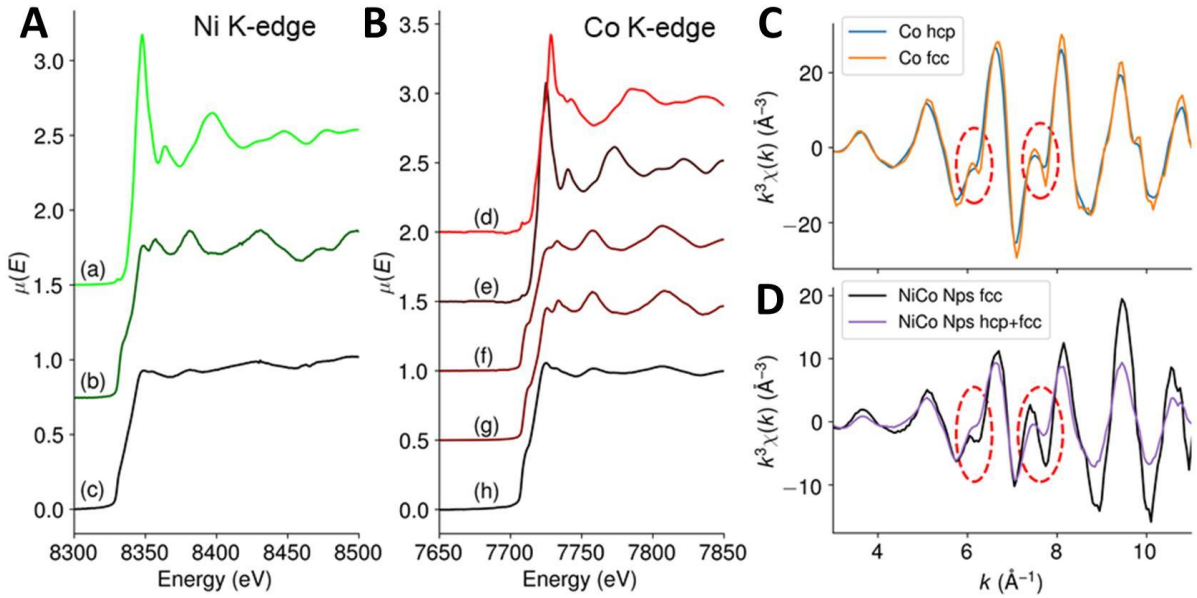


**Figure 3** (A) XANES of the *fcc* NiCo NPs at Ni K-edge, (a) NiO ref, (b) Ni(0) foil ref, (c) NiCo NPs. (B) XANES of the *fcc* NiCo NPs at Co K-edge, (d) $Co_3O_4$ ref, (e) CoO ref, (f) Co(0) *hcp* ref, (g) Co(0) *fcc* ref[40] and (h) NiCo NPs. (C, D) EXAFS at Co K-edge of (blue) Co *hcp*, (orange) Co *fcc*, (black) *fcc* NiCo NPs and (violet) *fcc*+*hcp* NiCo NPs. The red circles are a guide to the eye to point the features used to discriminate between Co *hcp* and *fcc* phases.

A slight variation of operating conditions might trigger the appearance of the Co *hcp* phase in some samples. Indeed, the nucleation of the metallic cobalt in the early stages occurs under kinetic control. Some variations come from irreducible process parameters at the lab scale: dissolution rate of the Co precursor grains, elimination rate of the carbonyl gas generated by the precursor decomposition, magnetic stirring efficiency, power surges applied by the heating mantle, etc. Others can be better controlled: ligand stoichiometry and temperature ramp. These two parameters were investigated next, using the diluted conditions, i.e. 22 equiv. of oleylamine.

### 2.3 Influence of TOP stoichiometry

We analyzed the impact of the phosphine ligand on the outcome of this reaction. Tri-*n*-octylphosphine easily coordinates to $Co_x(CO)_y$ species and forms various $Co_x(CO)_y(TOP)_z$

complexes which have been observed as intermediates in the synthesis of ε Co NPs.[41] These complexes may sequester part of the cobalt as molecular species in solution. Moreover, TOP is directly responsible for the phosphidization of the nanoparticles core. Therefore, we decided to synthetize NiCo NPs using lower amounts of TOP. When 1 equiv. of TOP was used, the nanoparticles were larger with a diameter of 20 nm (Figure S5D), as expected from a previous work.[33] However, the Co *hcp* cobalt phase still appeared in some samples (Figure S5C). Lowering further the amount of TOP to 0.8 equiv. diminished the signal intensity for the *hcp* phase in XRD, however the nanoparticles obtained were polydisperse and contained much bigger objects (Figure S6, C and D respectively). This suggested that some cobalt nucleated aside the preformed nickel nanoparticles under these conditions. Therefore, the following reactions were conducted with 1 equiv. of TOP, which means with the lower TOP amounts that still provided a fairly sharp size distribution for the nanoparticles.

### 2.4 Influence of temperature plateaus

Based on the observation made with 0.8 equiv. of TOP, it is possible that the *hcp* phase could come from isolated cobalt nanoparticles. The heteronucleation of cobalt species on the nickel nanoparticles (providing the desired core-shell structure) should present a lower activation energy than the homonucleation of cobalt in the solution. A too rapid heating ramp could allow both homo- and heteronucleation simultaneously. Rather, a more gentle heating, favoring the cobalt complex decomposition on the nanoparticle surface, may be adequate. Nucleation of cobalt species has been reported to begin at around 175 °C using $Co_2(CO)_8$ as organometallic precursor and TOPO as stabilizing agent.[42]. Therefore, we reduced the overall heating rate by adding two plateaus to the temperature program, at 140 °C and 160 °C. The resulting process is a ramp of 80 minutes instead of 40 minutes originally (Figure S1B).

When these conditions were used along with 1 equiv. of TOP, the hexagonal cobalt phase was not anymore detected by XRD (Figure 4A). An average Co/Ni ratio of 0.95 was detected by ICP-AES as an ensemble measurement (Table S3), very close to the introduced ratio of 1.0, which suggests that the loss of Co as molecular complexes was mostly suppressed under these conditions.

The nanoparticles were observed by TEM (Figure 4B). As the major species (95 % to 100 %, depending on the batches), 18 nm nanoparticles were observed. This diameter corresponds to the diameter for a core-shell structure built on 15 nm Ni nanoparticles (see Figure S7 and the geometrical model used for calculation in ESI section 11). We also noticed that these optimized conditions sometimes led to the presence of small quantities (less than 5 % in number) of larger 40 nm nanoparticles.

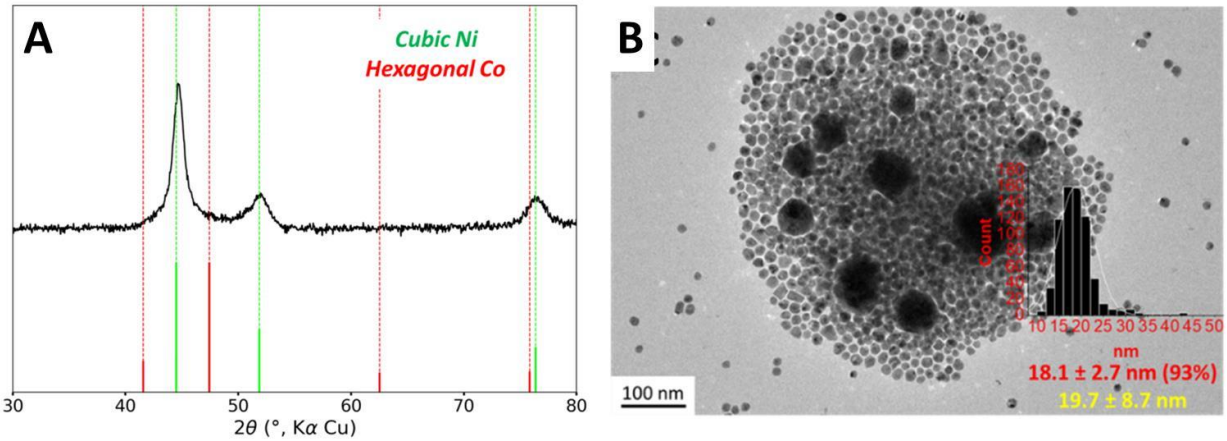


**Figure 4** (A) XRD pattern (the reference phase in green corresponds to *fcc* Ni, JCPDS file 00-004-0850, and the reference phase in red corresponds to *hcp* cobalt, JCPDS file 04-001-3273). (B) TEM, size distribution in the inset (average diameter in red is for the smaller nanoparticles (10-25 nm) and average diameter in yellow is for the whole population).

To analyze the composition of the larger nanoparticles, STEM-EDS measurements were performed (Figure 5). On the color-coded maps, the pixel intensity is linear vs. the photon counts, meaning that the lower concentrations of Co or Ni do not appear well when another region of the picture is highly concentrated in the same metal. The larger nanoparticles were rich in cobalt, with an average Co/Ni ratio between 10 and 35, depending on the particles.

This result suggests that the temperature plateaus were not able to suppress the homonucleation of cobalt nanoparticle. However, no *hcp* phase was observed by XRD, suggesting that under these conditions the Co crystallized as a *fcc* phase (of pure Co or NiCo alloy) even in the few larger nanoparticles present in the sample.

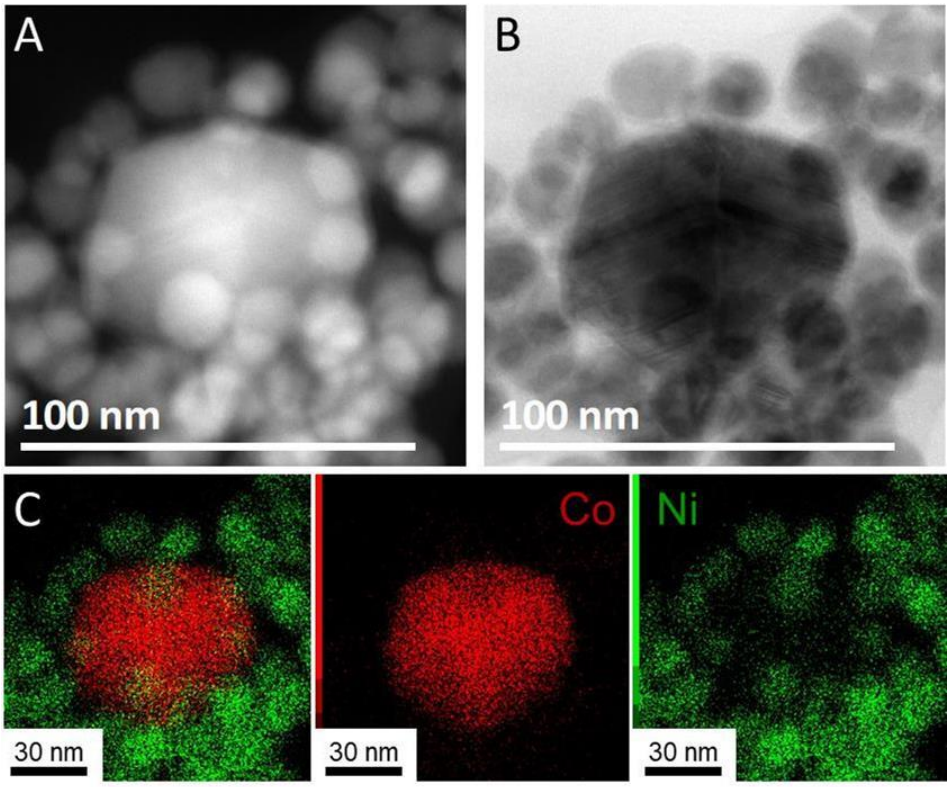


**Figure 5** (A) STEM bright field, (B) STEM–HAADF and (C) STEM–EDS mapping of NiCo NPs synthetized using 1 equiv. of TOP and temperature steps (red for cobalt and green for nickel).

The introduced Co/Ni ratio of 1:1 failed to provide solely the expected *fcc* core-shell nanoparticles. Thick shells seem to be difficult to form under these conditions. As a consequence, we performed reactions with lower amounts of cobalt in the hope to decrease the occurrence of larger cobalt-rich nanoparticles. Moreover, performing reactions with a low cobalt stoichiometry was an opportunity to better understand which were the preferential reaction sites for cobalt species.

### 2.5 Influence of cobalt stoichiometry and consequence on the surface

Using the long temperature program (80 min.) and 1 equiv. of TOP, the Co/Ni ratio was varied from 0.5 to 0.05. In none of this case was the *hcp* phase detected by XRD (Figure S10). Only the *fcc* phase was detected. Moreover, XANES at Co K-edge and Ni K-edge were very similar for the whole series of samples (Figure S9).

ICP-MS and ICP-AES confirmed that the ratio Co/Ni in the products follows the expected ratio (Figure 6B, blue circles and green squares, Table S3). This means that the reactions can be considered as quantitative *vs.* Ni and *vs.* Co under these reaction conditions.

TEM revealed again the presence of two populations of nanoparticles: the expected smaller ones (diameter between 10 and 25 nm), and larger ones (Figure S11 and Table S2, Figure S12). The occurrence of larger nanoparticles was only 3% with the lower Co/Ni ratio of 0.05. Two average diameters were calculated to describe this situation (Table S2): the regular average diameter taking into accounts all the nanoparticles and the average diameter of the small nanoparticles population. The first was poorly informative, as it came from a bimodal population. The second value allowed commenting on a more significant trend: as expected, larger average diameters were obtained with a larger amount of cobalt added at the second step: from 14.4 ± 2 nm (for 0.05 equiv. of Co) to 17.5 ± 3 nm (for 0.5 equiv. of Co) (Table S2).

We decided to evaluate the Co/Ni surface ratio by X-Ray photoelectron spectroscopy (XPS) (Figure 6A), keeping in mind that the few larger nanoparticles had a comparatively low contribution to this value. All spectra highlighted the presence of cobalt, cobalt oxide, nickel and nickel oxide (see fitting parameters in Table S1). The presence of surface oxides was expected considering the lack of stability of Ni(0) and Co(0) in air. The most appropriate region to calculate this ratio is the NiCo 3p region were Ni and Co are observed with very close binding energies, thus with the same inelastic mean free path of *ca* 2 nm.[43] Considering

that the cross sections are also very close for Ni and Co, the surface fraction for cobalt was calculated directly from the spectra as the fraction of the total area under Co 3p and Ni 3p: we thus plotted the Co/Ni surface ratio, as measured (Figure 6B, red dots). For samples with 0.05, 0.1 and 0.2 equiv. of Co *vs.* Ni, the experimental fractions of Co follow the introduced ones, consistent with the idea that most of the cobalt was deposited onto the preformed nickel nanoparticles. Above 0.5 equiv. of Co *vs.* Ni, the surface ratio was lower than expected, by comparison with the measurements by ICP (Figure 6B, green diamonds and blue triangles), suggesting that cobalt above 0.5 equiv. was not anymore covering the nickel. Rather, this was consistent with more and more cobalt being sequestered in large nanoparticles.

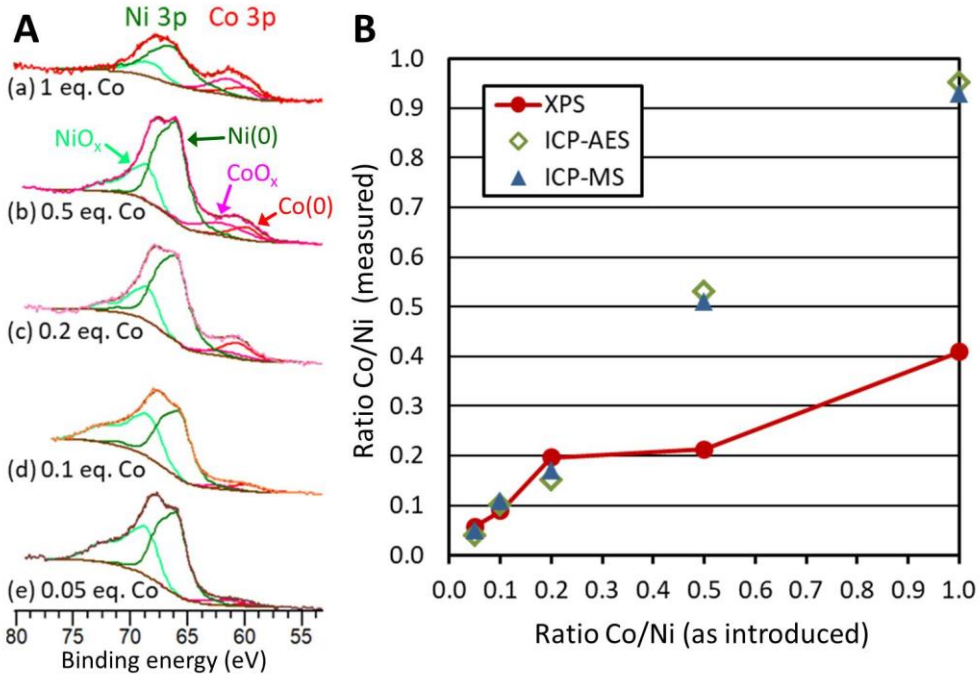


**Figure 6** (A) XPS NiCo 3p region of the NiCo NPs with decreasing stoichiometry of introduced cobalt (from 1 to 0.05 equiv. *vs.* Ni). Color code: Ni(0) in dark green, nickel oxide in light green, Co(0) in red, cobalt oxide in deep pink. (B) Ratio Co/Ni, as measured: at the surface from XPS peak areas (red dots), by ICP-MS (blue triangles), by ICP-AES (green diamonds).

STEM-EDS measurements (Figure 7A-D, complementary elemental maps are shown in Figure S13) provided more nuances insights on the final structure of the nanoparticles as well as on the steps of the cobalt reaction with nickel, when analysing the compositional maps

from smaller to larger Co amounts. Starting from the synthesis with lowest Co/Ni ratio (Figure 7A) we observed that initially cobalt nucleated preferentially on some of the Ni NPs but no large particles were observed at this stage. Increasing the Co/Ni ratio (Figure 7B and C) led to the formation of cobalt-rich zones in between the Ni NPs (circled in white on the Figure S13) as if Co started to grow preferentially in those areas where it is already abundant. Finally, when 0.5 equiv. of Co were used, large cobalt nanoparticles were more often present (not shown on the micrograph) along with core-shell NiCo nanoparticles (shown on Figure 7D).

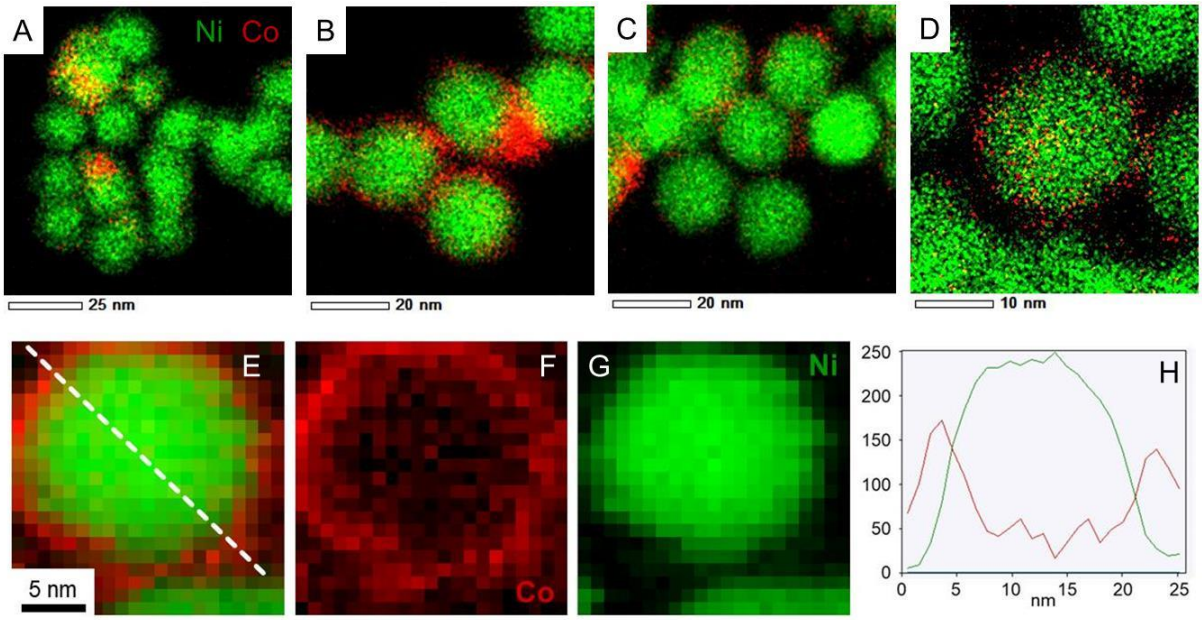


**Figure 7** (A–D) STEM–EDS overlay maps of NiCo with a variable Co *vs.* Ni ratio: (A) 0.05, (B) 0.1, (C) 0.2, (D) 0.5. (E–G) STEM–EELS measurement of a nanoparticle from the sample with Co/Ni = 0.1. (E) overlay, (F) Co L-edge signal, (G) Ni L-edge signal, (H) cross-section along the dotted line in (E).

EDS is a low-yield process, and as a result, STEM-EDS maps require fairly long exposure time. In order to confirm the core-shell structure of the nanoparticles and the absence of beam damage, electron energy loss spectroscopy (EELS) was employed (Figure 7E-H). It allows first, to collect the map in a faster way, and second, to avoid broadening effect of the probe in the material. As a result, a cartography with a resolution of 0.5 nm was obtained, for example

on the Co/Ni = 0.1 sample (Figure 7E). Both the filtered images and the cross-section (Figure 7H) confirm the core-shell structure of the nanoparticle, that is, a cobalt-rich outer region on top of a nickel-rich region. Due to the mobility of Co and Ni atoms in this binary compound,[44] there may be the presence of few Ni atoms in the shell region and few Co atoms in the core region.

## 3. Discussion

In the results showed above, we identified several key points in the synthesis of bimetallic nanoparticles. First, the reaction performed under concentrated conditions (12 equiv. of OAm *vs.* Ni, Table 1 entry 1) and with a fairly large amount of TOP (3 equiv.) was found to yield a significant phosphidation of the nickel core, and this, already at the first step of the reaction, prior to the addition of cobalt. The crystalline structure of the core was unchanged as a result of the second step (addition of 1 equiv. of Co), although partial substitution of Ni by Co in $Ni_{12}P_5$ would give a similar signature in XRD and cannot be excluded *a priori*.

The results of the first step stands in contrast with reactions forming *fcc* nickel nanoparticles reported at higher dilution and/or with lower amounts of phosphine.[33] It thus appears that the phosphine concentration (and not only the stoichiometry) is a key parameter to anticipate the nickel core phosphidation, which may start at temperatures as low as 150 °C during the reaction.[35,45] This seems in agreement with idea proposed in the literature that TOP and OAm compete as surface ligands:[36] TOP needs to stay coordinated long enough to the nickel surface for the P–C bond to be broken.

**Table 1 :** Summary of the operating conditions, phase and morphology observed through the study. Co, OAm and TOP are given in equiv. *vs.* Ni. Heating programs refer to these described in Figure S1.

| Entry | Section | Co | OAm | TOP | Heating program | Phase (XRD) | Morphology |
|---|---|---|---|---|---|---|---|
| **1** | 2.1 | 1 | 12 | 3.0 | short | $Ni_{12}P_5$ | single population, 12.4±1.2 nm |
| **2** | 2.2 | 1 | 22 | 3.0 | short | *fcc* or *fcc*+*hcp* | single population, 12.0±1.2 nm |
| **3** | 2.3 | 1 | 22 | 1.0 | short | *fcc* or *fcc*+*hcp* | single population, 20.3±2.2 nm |
| **4** | 2.3 | 1 | 22 | 0.8 | short | *fcc* or *fcc*+few *hcp* | two populations |
| **5** | 2.4 | 1 | 22 | 1.0 | long | *fcc* | major population (93%): 18.1±2.7 nm |
| **6** | 2.5 | 0.5 | 22 | 1.0 | long | *fcc* | major population (93%): 17.5±3 nm |
| **7** | 2.5 | 0.2 | 22 | 1.0 | long | *fcc* | major population (91%): 16.3±2.4 nm |
| **8** | 2.5 | 0.1 | 22 | 1.0 | long | *fcc* | major population (95%): 16.2±3 nm |
| **9** | 2.5 | 0.05 | 22 | 1.0 | long | *fcc* | major population (97%): 14.4±2 nm |

However, the actual mixture composition during and after the first step is more complex than a binary one. Indeed, we showed in a previous mechanistic work that the sole reaction of $Ni(acac)_2$ and OAm produces a range of species including water, keto-ene-amine and acetamide derived from OAm and acetylacetone secondary reactions, as depicted on Figure 8.[34] Thus, it is worth discussing in details all the experimental parameters that may affect the reaction outcome due to their variability. From a previous study on copper nanoparticles, we know that water forms in variable amounts from one synthesis to another and may further react with oxophilic metals.[46] Here, small amounts of water may affect the precise nature of reactions intermediates from $Co_2(CO)_8$ to metallic cobalt.

Moreover, water and some of the other byproducts are able to react with TOP upon heating, forming TOPO. This potentially lowers the available amount of TOP to stabilize

intermediate cobalt complexes in the second step, but also provides an additional surface ligand that may play a role in selecting the cobalt phase obtained at the end of the second heating step. TOPO was used for forming both *hcp* and $\varepsilon$ Co nanoparticles, starting from $Co_2(CO)_8$ as the cobalt precursor.[42,47] However, the $\varepsilon$ Co phase was stabilized only for nanoparticles below a few nanometers,[48,49] which explains why it was not encountered in the present study. Here, the amount of TOPO formed *in situ* would depend from the kinetics of side-reactions, thus on the heating ramp but also on the dead volume of the flask and other operating parameters such as the stirring speed.

Independently from the question of side-reactions, another parameter decreasing the reproducibility of the reactions is the presence of impurities in TOP batches: they vary in amount, from technical TOP to high-purity TOP, but also in nature from one manufacturer to the other. Actually, some works even used mixtures of technical and higher-purity TOP as a way to optimize the growth of cobalt nanoparticles.[48] We also know from our experience that TOP with purity higher than 90% but from different providers produces nickel nanoparticles with various diameters due to the presence of different impurities.[50]

Here, because TOP is involved both in the stabilization of intermediate Co complexes, or even clusters such as $[Co(CO)_2(TOP)_3]_3$,[37] and in the final size control of the nanoparticles, any variation on TOP nature and amount (affected by the possible formation of TOPO) may impact the outcome of the synthesis. For example, when only 0.8 equiv. of TOP was used (section 2.3, Table 1 entry 4), the stabilization of such species, which requires 3 TOP per Co, would have been disfavored. Lower TOP amounts resulted in the appearance of a number of large cobalt-rich nanoparticles that may have come from a secondary nucleation path directly from the solution rather than at the surface of existing nanoparticles. Moreover, the amount of available TOP is expected to directly affect the phase of the final nanoparticles: a study by de Silva et al. showed the role of intermediate clusters involving TOP, oleic acid and TOPO in

explaining mixture of *fcc* and *hcp vs.* the selective production of *fcc*, *hcp* or even $\varepsilon$ phases.[41] Overall, the complexity of the reaction mixture, in terms of the nature of the species present at each step and their relative amounts, is one key parameter explaining the sensitivity of the phase control in our reaction.

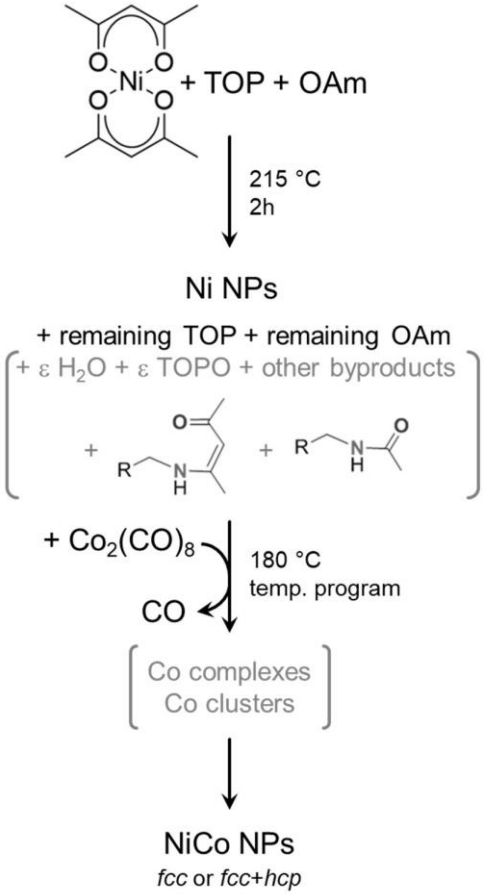


**Figure 8** Simplified reaction mechanism proposed for entries 2–9 of Table 1. The stoichiometries were omitted for clarity. Species in grey are not fully defined in amount or nature. In this scheme, ε indicates a small quantity of the species.

We also need to discuss the question of temperature control and heat power applied during the second heating step, after the addition of cobalt. Devices for temperature control vary from one laboratory to the other, as do the operating conditions (flask volume, heating mantle maximum power, parameters of the temperature control feedback, etc.). Even after a careful calibration, heating mantle and temperature control devices are never strictly equivalent. In most cases, this has no consequences on the reaction outcome: for example, in

the first step, the nucleation of Ni(0) is a sharp process happening only above 212 °C.[34] In the case of cobalt, the reaction is more delicate as it is strongly endothermic, and significantly affects the temperature of the mixture.[42] When the ramp was too fast, as in section 2.2 (Table 1 entries 2, 3 and 4), molecular processes of precursor decomposition, generation of reactive Co(0) species and crystallization may overlap, explaining a lack of repeatability. In contrast with this, introducing more temperature plateaus provides an empirical mean to better separate these processes.

We also should discuss the phase crystallization. In macroscopic compounds, *hcp* cobalt is expected to be a stable phase below 425 °C while *fcc* cobalt is the stable structure above this temperature.[32] For nanocrystals, these temperatures may have to be revised due to the low spatial extension of the crystals and the higher energetic contribution of the surface. In the present work, we may consider as a first approximation that *hcp* Co is the kinetic product while *fcc* Co is the thermodynamic one. This would explain in a satisfactory manner why the introduction of the several heating plateaus (section 2.4, Table 1 entry 5), providing more time for the intermediate to evolve, effectively suppressed the formation of the *hcp* phase.

So far, we have only discussed the reactions conducted with 1 equiv. of Co vs. Ni. This corresponds to a very large excess of cobalt species *vs.* available surface nickel sites, a situation that may favor the nucleation of cobalt inorganic compounds aside the existing nanoparticles. In other words, thick shells of cobalt are difficult to obtain when adding the whole amount of the highly reactive cobalt precursor at the same time. The use of a lower cobalt stoichiometry, down to 0.05, provides an opportunity to propose a reaction mechanism regarding how cobalt may cover the nickel nanoparticles (section 2.5, Table 1 entries 6 to 9).

Two points should be mentioned at this stage. First, Ni and Co are miscible in our reaction conditions,[38,51] meaning that the formation of cobalt-nickel gradient into the NPs top

layers cannot be excluded. Second, a previous study by *in situ* annealing in STEM-EDS revealed that Ni and Co alloying starts above 440 °C, a temperature well above the reaction temperature.[44] From these two facts, we retained a core-shell model for the NiCo NPs produced in section 2.5, while assuming that there could be a slight gradient at the interface of the Ni and Co. This proposition is consistent with STEM-EDS mapping of the nanoparticles (Figure 7). Regarding the phase, only the *fcc* one was obtained, regardless of the Co/Ni ratio, which is in contrast with another report using a higher reaction temperature (280 °C) and a different protocol.[29] Regarding the morphology, at the lower Co/Ni ratio of 0.05, we expected from our geometrical model (ESI section 10) that a full monolayer of Co cannot already be formed, as depicted on Figure 9. When increasing the stoichiometry of Co, it appeared that Co would start forming islands on the NiCo NPs while also nucleating as larger nanoparticles in the solution. The shell produced under these reaction conditions is thus not conformal to the starting nanoparticles, which is in agreement with previous observations using slightly different synthetic parameters.[11] The quantity of larger nanoparticles increased sensibly when increasing the cobalt stoichiometry, suggesting that the growth rate increases with the nanoparticles diameter and that the 'over growth' process is intrinsically hard to avoid in this synthetic design.

Besides, we propose that the larger nanoparticles form due to either a too high concentration of cobalt in the reaction medium when using the higher stoichiometries, and also possibly due to Ostwald ripening in the later stages of the temperature program. Indeed, for Co/Ni = 0.5, the cobalt would have to form at least 3 conformal monolayers if it was homogeneously deposited (Figure S7). Regarding this point, it may be useful to remove amines from the medium, as it may promote cobalt dissolution upon prolongated reaction times,[29] but this would mean a change in strategy for the first step of the reaction (the synthesis of the Ni NPs). As another perspective, further optimization of the protocol could

include a step-wise addition of Co (inspired from the SILAR method for the growth of quantum dots)[52] or using continuous flow microreactors[53] in order to obtain conformal core-shell nanoparticles with a single size-distribution. However, this will still represent a challenge, in particular regarding the very high sensitivity of the cobalt precursor, which decomposes rapidly at room temperature even under strict inert atmosphere, and the lack of colloidal stability of the NPs.

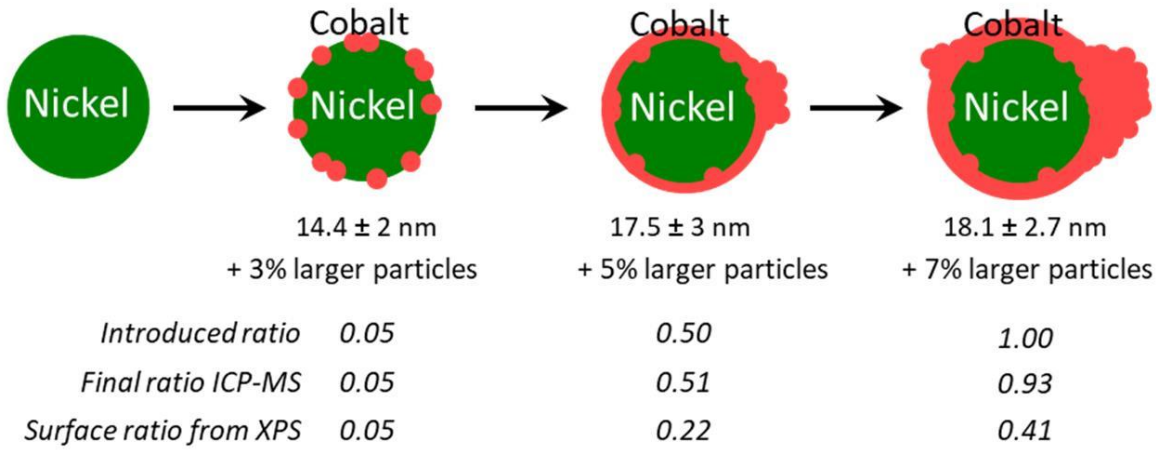


**Figure 9** Proposed mechanism for the cobalt reaction with the nickel nanonoparticles at selected stages. The bottom table recalls selected Co/Ni ratio. The top values recall the average diameters of the smaller NP population as well as the amount of larger NPs.

## 4. Conclusion

This work aimed to a better comprehension of the phenomena leading to the formation of *fcc* nickel cobalt nanoparticles. The apparently random presence of a Co *hcp* phase in the XRD of these nanoparticles raised the question of the high sensitivity of the protocol to small operating conditions. We tried to rationalize such observation by studying the effect of different parameters such as the amount of ligand or the heating program for the formation of the cobalt shell. The amount of TOP ligand utilized in this synthesis did not affect the crystallinity of the final nanoparticles while it affected greatly their shape and dimension. On the other hand, the use of a longer heating program for the deposition of the cobalt shell allowed the production of phase-pure *fcc* NiCo NPs.

Our experiments demonstrated that, when several temperature plateaus were used along with few equiv. of Co, the first cobalt layer was effectively deposited onto the Ni Nps. However, at higher Co/Ni ratio, thicker cobalt layer tended to grow on top of existing cobalt layer, and the formation of a second population of larger nanoparticles was observed as a byproduct. The sole criterion of phase purity was therefore not a good indicator of the final structure of the nanoparticles. Finally, we rationalized these observations in relation with the complexity of the reaction in terms of molecular species appearing both at the first and second step of the reaction, and we proposed a schematic growth mechanism for the cobalt domains.

There is no doubt that a full understanding of this seemingly simple protocol has yet to be reached by varying further operating conditions, such as the temperature of addition of the cobalt precursor, the absolute influence of cobalt concentration and possibly the use of alternative cobalt precursors. Preliminary attempts concerning the first point revealed that every degree counts when dealing with such highly reactive precursor. On a more general note, we call for a more systematic report of nanoparticles syntheses that are highly sensitive to operating conditions, because robustness is a key issue of nanotechnology developments.[54–56] Although these may have been so far flying under the radar, being sometimes considered as "negative results", this will be enlightening to the community as an effort to strengthen our protocols, and this will also be key to successful implementation of automated methods and analysis in NPs synthetic design, eg. using AI technologies. Moreover, our work suggests the relevance of more comprehensive studies of phase control for metallic core-shell nanoparticles that may adopt several combination of phases, in order to further exploit the catalytic and magnetic[51] properties of these objects.

**Acknowledgements**

This project has received funding from the European Research Council (ERC) under the European Union's Horizon 2020 research and innovation programme (grant agreement No 758480). Sorbonne Université, Collège de France and CNRS are acknowledged for support. Antoine Miche (Sorbonne Université, CNRS, Fédération de Chimie et Matériaux de Paris-Centre, LRS) is acknowledged for the XPS measurements. Elodie Barruet-Collard (NIMBE, CEA and CNRS) is acknowledged for ICP-MS and ICP-AES measurements. Sandra Casale (Sorbonne Université, CNRS, Fédération de Chimie et Matériaux de Paris-Centre) is acknowledged for HRTEM and EDS measurements. We acknowledge SOLEIL synchrotron for beamtime allocation on the SAMBA beamline under project 20191697, and we acknowledge Andrea Zitolo for help with the measurements on the beamline. The authors are grateful to the French METSA network (FR3507) for the financial support of the scanning transmission electron microscope experiments. Mounib Bahri (from IPCMS) is acknowledged for help with the preliminary measurements on the samples. We acknowledge Prof. D. Sprouster (Stony Brook University) for providing us with the data at Co K-edge of the Co *fcc* reference.

## 6. References

(1) Ya-Wen Zhang. Bimetallic Nanostructures: Shape-Controlled Synthesis for Catalysis, Plasmonics, and Sensing Applications. *Focus Catal.* **2018**, *2018* (9), 7. https://doi.org/10.1016/j.focat.2018.08.056.

(2) Anderson, D. L. Chemical Composition of the Mantle. *J. Geophys. Res.* **1983**, *88* (S01), B41. https://doi.org/10.1029/JB088iS01p00B41.

(3) San-José-Alonso, D.; Juan-Juan, J.; Illán-Gómez, M. J.; Román-Martínez, M. C. Ni, Co and Bimetallic Ni-Co Catalysts for the Dry Reforming of Methane. *Appl. Catal. A Gen.*

**2009**, *371* (1–2), 54–59. https://doi.org/10.1016/j.apcata.2009.09.026.

(4) Luisetto, I.; Tuti, S.; Di Bartolomeo, E. Co and Ni Supported on CeO2 as Selective Bimetallic Catalyst for Dry Reforming of Methane. *Int. J. Hydrogen Energy* **2012**, *37* (21), 15992–15999. https://doi.org/https://doi.org/10.1016/j.ijhydene.2012.08.006.

(5) AlSabban, B.; Falivene, L.; Kozlov, S. M.; Aguilar-Tapia, A.; Ould-Chikh, S.; Hazemann, J. L.; Cavallo, L.; Basset, J. M.; Takanabe, K. In-Operando Elucidation of Bimetallic CoNi Nanoparticles during High-Temperature CH4/CO2 Reaction. *Appl. Catal. B Environ.* **2017**, *213*, 177–189. https://doi.org/10.1016/j.apcatb.2017.04.076.

(6) Chou, C.-C.; Hsieh, C.-H.; Chen, B.-H. Hydrogen Generation from Catalytic Hydrolysis of Sodium Borohydride Using Bimetallic Ni–Co Nanoparticles on Reduced Graphene Oxide as Catalysts. *Energy* **2015**, *90*, 1973–1982. https://doi.org/https://doi.org/10.1016/j.energy.2015.07.023.

(7) Chen, B.; Li, F.; Yuan, G. Highly Stable and Recyclable Graphene Layers Protected Nickel–Cobalt Bimetallic Nanoparticles as Tunable Hydrotreating Catalysts for Phenylpropane Linkages in Lignin. *Catal. Letters* **2017**, *147* (11), 2877–2885. https://doi.org/10.1007/s10562-017-2179-1.

(8) Mohammad, S. A.; Shingdilwar, S.; Banerjee, S. Recoverable and Recyclable Nickel–Cobalt Magnetic Alloy Nanoparticle Catalyzed Reversible Deactivation Radical Polymerization of Methyl Methacrylate at 25 °C. *Polym. Chem.* **2020**, *11* (2), 287–291. https://doi.org/10.1039/C9PY00942F.

(9) Palazzolo, A.; Carenco, S. Phosphines Modulating the Catalytic Silane Activation on Nickel–Cobalt Nanoparticles, Tentatively Attributed to Frustrated Lewis Pairs in a Colloidal Solution. *Chem. Mater.* **2021**, *33* (19), 7914–7922. https://doi.org/10.1021/acs.chemmater.1c03105.

(10) Kotel'nikova, S. V.; Suslonov, V. V.; Bobrysheva, N. P.; Osmolowsky, M. G.;

Osmolowskaya, O. M. Synthesis of Bimetallic Nanoparticles Based on Cobalt and Nickel. Effects of Their Composition and Structure on Catalytic and Magnetic Properties. *Russ. J. Gen. Chem.* **2017**, *87* (5), 1093–1094. https://doi.org/10.1134/S1070363217050334.

(11) Carenco, S.; Wu, C.-H.; Shavorskiy, A.; Alayoglu, S.; Somorjai, G. A.; Bluhm, H.; Salmeron, M. Synthesis and Structural Evolution of Nickel–Cobalt Nanoparticles Under H2 and CO2. *Small* **2015**, *11* (25), 3045–3053. https://doi.org/10.1002/smll.201402795.

(12) Yu, Y.; Jin, G.; Wang, Y.; Guo, X. Synthesis of Natural Gas from CO Methanation over SiC Supported Ni–Co Bimetallic Catalysts. *Catal. Commun.* **2013**, *31*, 5–10. https://doi.org/10.1016/j.catcom.2012.11.005.

(13) Wang, J.; Liu, Y.; Cheng, L.; Chen, R.; Ni, H. Quasi-Aligned Nanorod Arrays Composed of Nickel–Cobalt Nanoparticles Anchored on TiO2/C Nanofiber Arrays as Free Standing Electrode for Enzymeless Glucose Sensors. *J. Alloys Compd.* **2020**, *821*, 153510. https://doi.org/10.1016/j.jallcom.2019.153510.

(14) Hosseini, S. G.; Gholami, S.; Mahyari, M. Superb Catalytic Properties of Nickel Cobalt Bimetallic Nanoparticles Immobilized on 3D Nitrogen-Doped Graphene for Thermal Decomposition of Ammonium Perchlorate. *Res. Chem. Intermed.* **2019**, *45* (3), 1527–1543. https://doi.org/10.1007/s11164-018-3677-5.

(15) Ciotonea, C.; Hammi, N.; Dhainaut, J.; Marinova, M.; Ungureanu, A.; El Kadib, A.; Michon, C.; Royer, S. Phyllosilicate-derived Nickel-cobalt Bimetallic Nanoparticles for the Catalytic Hydrogenation of Imines, Oximes and N-heteroarenes. *ChemCatChem* **2020**, *12* (18), 4652–4663. https://doi.org/10.1002/cctc.202000704.

(16) Yamauchi, T.; Tsukahara, Y.; Yamada, K.; Sakata, T.; Wada, Y. Nucleation and Growth of Magnetic Ni−Co (Core−Shell) Nanoparticles in a One-Pot Reaction under

Microwave Irradiation. *Chem. Mater.* **2011**, *23* (1), 75–84. https://doi.org/10.1021/cm102255j.

(17) Sciortino, L.; Giannici, F.; Martorana, A.; Ruggirello, A. M.; Liveri, V. T.; Portale, G.; Casaletto, M. P.; Longo, A. Structural Characterization of Surfactant-Coated Bimetallic Cobalt/Nickel Nanoclusters by XPS, EXAFS, WAXS, and SAXS. *J. Phys. Chem. C* **2011**, *115* (14), 6360–6366. https://doi.org/10.1021/jp200288y.

(18) Ung, D.; Soumare, Y.; Chakroune, N.; Viau, G.; Vaulay, M.-J.; Richard, V.; Fiévet, F. Growth of Magnetic Nanowires and Nanodumbbells in Liquid Polyol. *Chem. Mater.* **2007**, *19* (8), 2084–2094. https://doi.org/10.1021/cm0627387.

(19) Sharma, S.; Gajbhiye, N. S.; Ningthoujam, R. S. Synthesis and Self-Assembly of Monodisperse CoxNi100−x (X=50,80) Colloidal Nanoparticles by Homogenous Nucleation. *J. Colloid Interface Sci.* **2010**, *351* (2), 323–329. https://doi.org/10.1016/j.jcis.2010.07.065.

(20) Usami, T.; Salman, S. A.; Kuroda, K.; Gouda, M. K.; Mahdy, A.; Okido, M. Synthesis of Cobalt-Nickel Nanoparticles via a Liquid-Phase Reduction Process. *J. Nanotechnol.* **2021**, *2021*, 1–7. https://doi.org/10.1155/2021/9401024.

(21) Almomani, F.; Bhosale, R. R. Nickel/Cobalt Nanoparticles for Electrochemical Production of Hydrogen. *Int. J. Hydrogen Energy* **2021**, *46* (20), 11369–11377. https://doi.org/10.1016/j.ijhydene.2020.04.229.

(22) Gan, W.; Wu, L.; Wang, Y.; Gao, H.; Gao, L.; Xiao, S.; Liu, J.; Xie, Y.; Li, T.; Li, J. Carbonized Wood Decorated with Cobalt-Nickel Binary Nanoparticles as a Low-Cost and Efficient Electrode for Water Splitting. *Adv. Funct. Mater.* **2021**, *31* (29), 2010951. https://doi.org/10.1002/adfm.202010951.

(23) Yun, R.; Hong, L.; Ma, W.; Wang, S.; Zheng, B. Nitrogen-Rich Porous Carbon-Stabilized Ni–Co Nanoparticles for the Hydrogenation of Quinolines. *ACS Appl. Nano*

*Mater.* **2019**, *2* (10), 6763–6768. https://doi.org/10.1021/acsanm.9b01702.

(24) Hernández Mejía, C.; van der Hoeven, J. E. S.; de Jongh, P. E.; de Jong, K. P. Cobalt–Nickel Nanoparticles Supported on Reducible Oxides as Fischer–Tropsch Catalysts. *ACS Catal.* **2020**, *10* (13), 7343–7354. https://doi.org/10.1021/acscatal.0c00777.

(25) Dahonog, L. A.; Balela, M. D. L. Electroless Deposition of Nickel-Cobalt Nanoparticles for Hydrogen Evolution Reaction. *Mater. Today Proc.* **2020**, *22*, 268–274. https://doi.org/10.1016/j.matpr.2019.08.116.

(26) Zhang, J.; Lan, C. Q. Nickel and Cobalt Nanoparticles Produced by Laser Ablation of Solids in Organic Solution. *Mater. Lett.* **2008**, *62* (10–11), 1521–1524. https://doi.org/10.1016/j.matlet.2007.09.038.

(27) Garbarino, G.; Cavattoni, T.; Riani, P.; Brescia, R.; Canepa, F.; Busca, G. On the Role of Support in Metallic Heterogeneous Catalysis: A Study of Unsupported Nickel–Cobalt Alloy Nanoparticles in Ethanol Steam Reforming. *Catal. Letters* **2019**, *149* (4), 929–941. https://doi.org/10.1007/s10562-019-02688-9.

(28) Ahmed, J.; Sharma, S.; Ramanujachary, K. V.; Lofland, S. E.; Ganguli, A. K. Microemulsion-Mediated Synthesis of Cobalt (Pure Fcc and Hexagonal Phases) and Cobalt–Nickel Alloy Nanoparticles. *J. Colloid Interface Sci.* **2009**, *336* (2), 814–819. https://doi.org/10.1016/j.jcis.2009.04.062.

(29) van Schooneveld, M. M.; Campos-Cuerva, C.; Pet, J.; Meeldijk, J. D.; van Rijssel, J.; Meijerink, A.; Erné, B. H.; de Groot, F. M. F. Composition Tunable Cobalt–Nickel and Cobalt–Iron Alloy Nanoparticles below 10 Nm Synthesized Using Acetonated Cobalt Carbonyl. *J. Nanoparticle Res.* **2012**, *14* (8), 991. https://doi.org/10.1007/s11051-012-0991-5.

(30) Marusak, K. E.; Johnston-Peck, A. C.; Wu, W. C.; Anderson, B. D.; Tracy, J. B. Size and Composition Control of CoNi Nanoparticles and Their Conversion into

Phosphides. *Chem. Mater.* **2017**, *29* (7), 2739–2747. https://doi.org/10.1021/acs.chemmater.6b04335.

(31) López-Tinoco, J.; Mendoza-Cruz, R.; Bazán-Díaz, L.; Karuturi, S. C.; Martinelli, M.; Cronauer, D. C.; Kropf, A. J.; Marshall, C. L.; Jacobs, G. The Preparation and Characterization of Co–Ni Nanoparticles and the Testing of a Heterogenized Co–Ni/Alumina Catalyst for CO Hydrogenation. *Catalysts* **2019**, *10* (1), 18. https://doi.org/10.3390/catal10010018.

(32) Sun, S.; Murray, C. B. Synthesis of Monodisperse Cobalt Nanocrystals and Their Assembly into Magnetic Superlattices (Invited). *J. Appl. Phys.* **1999**, *85* (8), 4325–4330. https://doi.org/10.1063/1.370357.

(33) Carenco, S.; Boissière, C.; Nicole, L.; Sanchez, C.; Le Floch, P.; Mézailles, N. Controlled Design of Size-Tunable Monodisperse Nickel Nanoparticles. *Chem. Mater.* **2010**, *22* (4), 1340–1349. https://doi.org/10.1021/cm902007g.

(34) Carenco, S.; Labouille, S.; Bouchonnet, S.; Boissière, C.; Le Goff, X. F.; Sanchez, C.; Mézailles, N. Revisiting the Molecular Roots of a Ubiquitously Successful Synthesis: Nickel(0) Nanoparticles by Reduction of [Ni(Acetylacetonate) 2]. *Chem. - A Eur. J.* **2012**, *18* (44), 14165–14173. https://doi.org/10.1002/chem.201201071.

(35) Carenco, S.; Liu, Z.; Salmeron, M. The Birth of Nickel Phosphide Catalysts: Monitoring Phosphorus Insertion into Nickel. *ChemCatChem* **2017**, *9* (12), 2318–2323. https://doi.org/10.1002/cctc.201601526.

(36) Muthuswamy, E.; Savithra, G. H. L.; Brock, S. L. Synthetic Levers Enabling Independent Control of Phase, Size, and Morphology in Nickel Phosphide Nanoparticles. *ACS Nano* **2011**, *5* (3), 2402–2411. https://doi.org/10.1021/nn1033357.

(37) Pregaglia, G. F.; Andreetta, A.; Ferrari, G. F.; Montrasi, G.; Ugo, R. Catalysis by Phosphine Cobalt Carbonyl Complexes. III. The Synthesis and Catalytic Properties of a

New Series of Cobalt(0) Clusters. *J. Organomet. Chem.* **1971**, *33* (1), 73–87. https://doi.org/10.1016/S0022-328X(00)80805-0.

(38) Baker, H. *ASM Handbook: Alloy Phase Diagrams, Vol. 3*; Materials Park, Ohio, 1992.

(39) Sprouster, D. J.; Ridgway, M. C. Ion Beam Formation and Modification of Cobalt Nanoparticles. *Appl. Sci.* **2012**, *2* (2), 396–442. https://doi.org/10.3390/app2020396.

(40) Sprouster, D. J.; Giulian, R.; Araujo, L. L.; Kluth, P.; Johannessen, B.; Cookson, D. J.; Foran, G. J.; Ridgway, M. C. Structural and Vibrational Properties of Co Nanoparticles Formed by Ion Implantation. *J. Appl. Phys.* **2010**, *107* (1), 014313. https://doi.org/10.1063/1.3275052.

(41) de Silva, R. M.; Palshin, V.; de Silva, K. M. N.; Henry, L. L.; Kumar, C. S. S. R. A New Role for Surfactants in the Formation of Cobalt Nanoparticles. *J. Mater. Chem.* **2008**, *18* (7), 738. https://doi.org/10.1039/b714456c.

(42) Timonen, J. V. I.; Seppälä, E. T.; Ikkala, O.; Ras, R. H. A. From Hot-Injection Synthesis to Heating-Up Synthesis of Cobalt Nanoparticles: Observation of Kinetically Controllable Nucleation. *Angew. Chemie Int. Ed.* **2011**, *50* (9), 2080–2084. https://doi.org/10.1002/anie.201005600.

(43) Tanuma, S.; Powell, C. J.; Penn, D. R. Calculation of Electron Inelastic Mean Free Paths (IMFPs) VII. Reliability of the TPP-2M IMFP Predictive Equation. *Surf. Interface Anal.* **2003**, *35* (3), 268–275. https://doi.org/10.1002/sia.1526.

(44) Bonifacio, C. S.; Carenco, S.; Wu, C. H.; House, S. D.; Bluhm, H.; Yang, J. C. Thermal Stability of Core-Shell Nanoparticles: A Combined in Situ Study by XPS and TEM. *Chem. Mater.* **2015**, *27* (20), 6960–6968. https://doi.org/10.1021/acs.chemmater.5b01862.

(45) García-Muelas, R.; Li, Q.; López, N. Initial Stages in the Formation of Nickel Phosphides. *J. Phys. Chem. B* **2018**, *122* (2), 672–678.

https://doi.org/10.1021/acs.jpcb.7b06020.

(46) Pesesse, A.; Carenco, S. Influence of the Copper Precursor on the Catalytic Transformation of Oleylamine during Cu Nanoparticle Synthesis. *Catal. Sci. Technol.* **2021**, *11* (15), 5310–5320. https://doi.org/10.1039/D1CY00639H.

(47) Puntes, V. F.; Krishnan, K. M.; Alivisatos, A. P. Colloidal Nanocrystal Shape and Size Control: The Case of Cobalt. *Science (80-. ).* **2001**, *291* (5511), 2115–2117. https://doi.org/10.1126/science.1057553.

(48) Puntes, V. F.; Krishnan, K. M.; Alivisatos, P. Synthesis, Self-Assembly, and Magnetic Behavior of a Two-Dimensional Superlattice of Single-Crystal ε-Co Nanoparticles. *Appl. Phys. Lett.* **2001**, *78* (15), 2187–2189. https://doi.org/10.1063/1.1362333.

(49) Dassenoy, F.; Casanove, M.-J.; Lecante, P.; Verelst, M.; Snoeck, E.; Mosset, A.; Ely, T. O.; Amiens, C.; Chaudret, B. Experimental Evidence of Structural Evolution in Ultrafine Cobalt Particles Stabilized in Different Polymers—From a Polytetrahedral Arrangement to the Hexagonal Structure. *J. Chem. Phys.* **2000**, *112* (18), 8137–8145. https://doi.org/10.1063/1.481414.

(50) Carenco, S. PhD Thesis. A New Versatile Route to Metal Phosphide Nanoparticules Using White Phosphorus : Applications in Catalysis and for Lithium Batteries, UPMC, 2011.

(51) Guisbiers, G.; Mendoza-Perez, R. Magnetic, Thermal and Martensitic Phase Transitions in Ni–Co Nanoparticles. *Nanotechnology* **2020**, *31* (29), 295702. https://doi.org/10.1088/1361-6528/ab88ef.

(52) Narayanaswamy, A.; Feiner, L. F.; Meijerink, A.; van der Zaag, P. J. The Effect of Temperature and Dot Size on the Spectral Properties of Colloidal InP/ZnS Core-Shell Quantum Dots. *ACS Nano* **2009**, *3* (9), 2539–2546. https://doi.org/10.1021/nn9004507.

(53) Baek, J.; Allen, P. M.; Bawendi, M. G.; Jensen, K. F. Investigation of Indium

Phosphide Nanocrystal Synthesis Using a High-Temperature and High-Pressure Continuous Flow Microreactor. *Angew. Chem. Int. Ed. Engl.* **2011**, *50* (3), 627–630. https://doi.org/10.1002/anie.201006412.

(54) Leong, H. S.; Butler, K. S.; Brinker, C. J.; Azzawi, M.; Conlan, S.; Dufés, C.; Owen, A.; Rannard, S.; Scott, C.; Chen, C.; et al. On the Issue of Transparency and Reproducibility in Nanomedicine. *Nat. Nanotechnol.* **2019**, *14* (7), 629–635. https://doi.org/10.1038/s41565-019-0496-9.

(55) Baer, D. R. The Chameleon Effect: Characterization Challenges Due to the Variability of Nanoparticles and Their Surfaces. *Front. Chem.* **2018**, *6*. https://doi.org/10.3389/fchem.2018.00145.

(56) Ovejero, J. G.; Gallo-Cordova, A.; Roca, A. G.; Morales, M. P.; Veintemillas-Verdaguer, S. Reproducibility and Scalability of Magnetic Nanoheater Synthesis. *Nanomaterials* **2021**, *11* (8), 2059. https://doi.org/10.3390/nano11082059.

# Table of Content Entry